

Spreading of Low-viscosity Ink Filaments Driven by Bath Viscoelasticity in Embedded Printing

Jae Hyung Cho and Emilie Dressaire*

Department of Mechanical Engineering, University of California, Santa Barbara, California 93106, USA

(Dated: September 25, 2024)

Inks deposited in conventional direct ink writing need to be able to support their own weight and that of the upper layers with minimal deformation to preserve the structural integrity of the three-dimensional (3D) printed parts. This constraint limits the range of usable inks to high-viscosity materials. Embedded printing enables the use of much softer inks by depositing the materials in a bath of another fluid that provides external support, thus diversifying the types of 3D printable structures. The interactions between the ink and bath fluids, however, give rise to a unique type of defect: spreading of the dispensed ink behind the moving nozzle. By printing horizontal threads made of dyed water in baths of Carbopol suspensions, we demonstrate that the spreading can be attributed to the pressure field generated in the viscous bath by the relative motion of the nozzle. As the pressure gradient increases with the viscosity of the bath fluid while the viscosity of the ink resists the flow, a larger bath-to-ink viscosity ratio results in more spreading for low-concentration Carbopol baths. For high-concentration, yield-stress-fluid baths, we find that the steady-state viscosity alone cannot account for the spreading, as the elastic stress becomes comparable to the viscous stress and the bath fluid around the dispensed ink undergoes fluidization and resolidification. By parameterizing the transient rheology of the high-concentration Carbopol suspensions using a simple viscoelastic model, we suggest that the ink spreading is exacerbated by the elasticity but is mitigated by the yield stress as long as the yield stress is low enough to allow steady injection of the ink. These results help illuminate the link between the bath rheology and the printing quality in embedded 3D printing.

I. INTRODUCTION

The geometry of three-dimensional (3D) structures built via conventional direct ink writing is inherently constrained by the effect of gravity; the ink has to be dispensed onto previously deposited filaments, and these filaments have to be sufficiently stiff to support the parts that lie above themselves [1, 2]. Embedded 3D printing opens up a range of printable geometries by dispensing the ink in a bath of viscous fluid. The bath fluid holds the dispensed ink filament in place against the gravity, thus having the ink “embedded” in its matrix [3–26]. Removing the need to stack up printed filaments enables fabrication of delicate structures, such as overhangs, and renders runny ink fluids that cannot otherwise retain their own shapes compatible with direct ink writing. Use of less stiff, low-viscosity fluids as inks may be desirable especially in bioprinting. Lower ink viscosity decreases the injection pressure, which induces a lower stress field that cells in the ink would have to withstand during the flow, hence improving the cell viability within the printed structure [18, 23].

The presence of the bath fluid in embedded printing, however, gives rise to a unique type of structural defect – ink spreading behind the nozzle. Such spreading of the ink can be readily observed by injecting a low-viscosity fluid into a bath of another fluid while the nozzle translates in a direction perpendicular to its orientation, as

shown in Fig. 1(a). For more viscous inks, similar phenomena, such as the vertical displacement of printed filaments [6, 12, 13, 19, 22] or the vertical elongation of the filament cross section [14, 21, 22, 24, 27], have been reported. The origin of the upward driving force, however, remains largely unexplained.

The upward ink flow behind the nozzle is driven by a nontrivial flow of the surrounding bath fluid, often compounded by its complex rheological properties. For a Newtonian fluid, the momentum equation of the flow past an infinite cylinder in the viscosity-dominated regime cannot be solved without including an advective inertial term [28]. The flow of a viscoelastic fluid around a cylinder features pressure and velocity fields highly sensitive to the relative magnitudes of the viscous and the elastic forces [29–31]. The flow of a yield stress fluid that exhibits solidlike deformations below a stress threshold displays pronounced spatial heterogeneities, as the fluid is locally fluidized around the cylinder [32–34]. Embedded printing involves multiple factors that further complicate the flow, such as the end effect at the tip of the nozzle [31], physicochemical interactions between the ink and the bath fluids [16, 23, 27], elastoplastic deformations of the unyielded regions of the yield stress fluids [35], and flow-history dependence of the rheological parameters of thixotropic fluids [36, 37]. Given this complexity, one possible approach is to investigate how a selected group of key rheological material functions affects the phenomenon in a relatively simple model system.

In this work, we explore how the viscoelasticity of the bath fluid governs the ink spreading by printing straight, horizontal filaments of dyed water in baths of aqueous

* To whom correspondence should be addressed.
dressaire@ucsb.edu

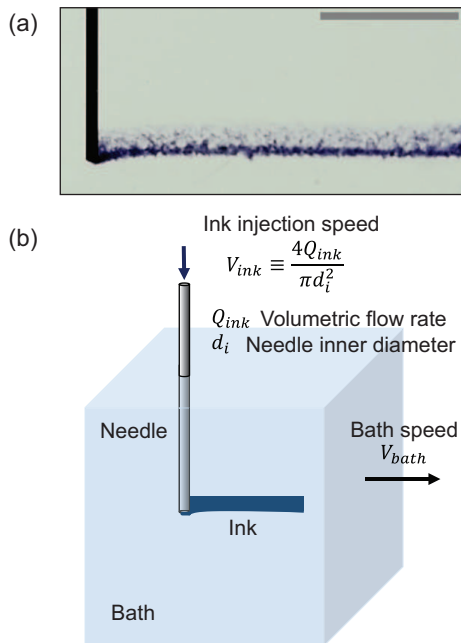


FIG. 1. (a) Vertical spreading of ink observed in embedded printing. As the nozzle translates to the left, the ink in the deposited horizontal thread partially spreads upward right behind the needle, forming an undesirable thin layer. Scale bar represents 10 mm. (b) Schematic of the experimental setup.

Carbopol suspensions. Extensively used as bath fluids because of their optical transparency and rheological tunability, Carbopol suspensions are mixtures of water and polyacrylic-acid-based microgel particles that can serve as a model shear thinning fluid at low concentrations and a model yield stress fluid at high concentrations [36, 38–41]. At low concentrations, the microgel particles are free to move around under shear, giving rise to shear-thinning behavior typical of suspensions whose particles interact hydrodynamically. At high concentrations, the microgel particles are jammed against each other, forming an elastic, space-spanning network of particles that induces a nonzero yield stress at the macroscopic level [38, 41]. Far less viscous than typical ink materials, water as the ink can effectively spread due to the force applied by the Carbopol suspension in either concentration regime, thus enabling us to readily quantify the defect behind the nozzle. Moreover, the Newtonian nature of water allows itself to be fully characterized by a single material function – a constant shear viscosity – which facilitates identification of any correlations between the ink spreading and the bath fluid rheology. As the Carbopol suspension is also primarily composed of water, we neglect the effects of the interfacial tension [42–44].

Our study identifies different spreading regimes depending on the concentration of the Carbopol suspensions. For Carbopol suspensions at low concentrations without yield stress, we find that the pressure drop across the nozzle due to the viscous flow of the bath fluid dictates the ink spreading. While a fluid element that travels around the nozzle undergoes a viscous pressure drop,

an element that travels unperturbed below the tip of the nozzle is subject to a constant pressure. The resultant pressure gradient in the nozzle direction causes the length of spreading to scale as the square root of the bath-to-ink viscosity ratio. For Carbopol suspensions at high concentrations that exhibit nonzero yield stress, we suggest that the pressure field behind the nozzle is set by the elasticity as well as the viscosity of the bath fluid. The ink flow within the yielded region of the bath behind the translating nozzle is subject to stresses caused by both the viscous flow and the elastic deformation of the surrounding matrix. Plus, the bath fluid behind the nozzle constantly undergoes a fluid-to-solid transition as the microgel particles arrange themselves to recover a force-bearing network [38, 41]. Using a set of model parameters that describe the transient state, we indeed identify comparable scales of the pressure gradients induced by the viscosity and the elasticity. The spreading at the high concentrations, however, is substantially less severe than that predicted by the viscoelasticity alone, and even decreases with the concentration for the most concentrated baths. We speculate that the decrease in the area of fluidization around the nozzle due to higher yield stress [9, 33] suppresses the viscous ink flow for these concentrations.

Although the results may seem to suggest that the ink spreading in embedded printing is best controlled by utilizing Carbopol suspensions at very low or very high concentrations, we demonstrate that other types of defects may arise at such extreme concentrations. At the lowest concentrations, the low viscosity of the bath fluid proves insufficient to hold the printed filaments in place, whereas at the highest concentrations, the high yield stress, coupled with the mechanical compliance of the ink injection system, gives rise to intermittent dispensing of the ink. By documenting the structural defects observed in embedding printing with a low-viscosity ink, our study provides a guideline for optimizing the material rheology and print speed as well as predicting the spread of the ink.

II. EXPERIMENTAL METHODS

A. Material preparation

To prepare a bath fluid, we add a specified amount of dry Carbopol powder (Carbopol 940 or Carbopol ETD 2050, Lubrizol) to 40 mL of purified water (Milli-Q purification system, Millipore Sigma), and magnetically stir the sample for over 16 h at room temperature to ensure complete mixing. We transfer the sample to a $40 \times 40 \times 40$ mm³ acrylic cube, and add 1 M aqueous sodium hydroxide (NaOH) solution dropwise to neutralize the acidic mixture. The sample is homogenized through mechanical stirring with an overhead mixer at 40 rev min⁻¹ for approximately 5 min. The rotation speed of the mixer is kept small to avoid trapping air bubbles in the Carbopol suspension. We let the sample

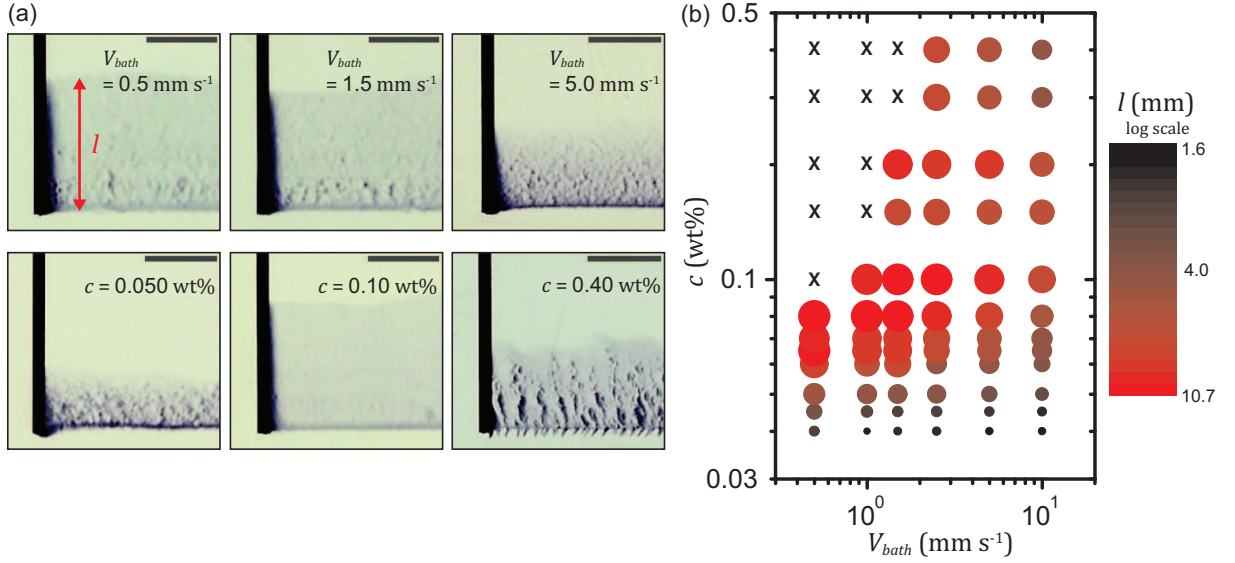


FIG. 2. (a) Spreading of dyed water ink in Carbopol 940 baths for different bath speeds V_{bath} at a concentration $c = 0.070$ wt% (top row) and for different concentrations c at a bath speed $V_{bath} = 5.0 \text{ mm s}^{-1}$ (bottom row). The penetration length of the ink in the needle direction is labeled as l . Each scale bar denotes 5 mm. (b) Penetration length l for different Carbopol 940 concentrations c and different bath speeds V_{bath} . The redder and the larger the circle, the higher the corresponding value of the penetration length. l tends to decrease monotonically with V_{bath} , while it peaks at intermediate concentrations as a function of c . Symbol \times indicates a highly unsteady ink flow, for which the mean penetration length cannot be reliably measured.

sit at least for 24 h before printing to minimize any possible effects of shear history formed during mixing and to further improve the homogeneity by the diffusion of the ions.

For the ink, we prepare a 0.1 wt% aqueous solution of a synthetic dye (Nigrosin, Sigma-Aldrich) by dissolving the dye in purified water under magnetic stirring for 5 min at room temperature. Given the low concentration of the solution, we assume that the viscosity of the ink is the same as that of pure water, $\eta_{ink} = 1.0 \text{ mPa s}$.

B. Embedded printing

We mount a cubic bath of Carbopol suspension onto a set of two perpendicularly connected ballscrew linear rails equipped with NEMA 17 stepper motors to move the bath in the vertical and a horizontal directions. In all our experiments, we move the bath only in the horizontal direction at a speed $V_{bath} = 0.5 - 10.0 \text{ mm s}^{-1}$, while a 20-gauge stainless steel needle (inner diameter $d_i = 0.603 \text{ mm}$, outer diameter $d_o = 0.908 \text{ mm}$) with a hydrophobic coating (LGN-GCC02, Liquid Glass) is held stationary in a vertical position, as shown in Fig. 1(b). The hydrophobic coating prevents any potential spreading driven by interfacial affinity between the needle and water. The needle is connected to a 10 mL syringe on a syringe pump (KD Scientific) that dispenses the ink at a fixed volumetric flow rate Q_{ink} , which corresponds to the average ink injection speed $V_{ink} \equiv 4Q_{ink}/(\pi d_i^2)$. The ink injection speed V_{ink} is kept the same as the bath translation speed V_{bath} , such that the volume of dispensed

ink per unit length of the filament stays constant. The spreading occurs without delay right behind the needle on the timescale of the bath translation, orders of magnitude smaller than the ink diffusion timescale.

The printing process is recorded using a DSLR camera (Nikon D5300) equipped with a 105 mm macro lens and an LED backlight panel (Phlox) for illumination. During the recording, the walls of the acrylic cube remain perpendicular to the optical path of the lens to minimize optical distortion due to refraction. We limit our analysis of the printing dynamics to its steady state by neglecting the transient behaviors at the beginning or the end of the bath translation. The vertical length of the spread ink layer in the steady state, measured from the tip of the needle, is denoted by the penetration length l , as displayed in Fig. 2(a).

C. Rheometry

We use a stress-controlled rotational rheometer (MCR 92, Anton Paar) for rheological characterization of the Carbopol suspension bath fluid. To minimize wall slip, a sandblasted 50 mm diameter plate-plate geometry is used at a gap size of $500 \text{ }\mu\text{m}$. Each experiment starts with a preshear in both positive and negative directions performed at a shear rate $\dot{\gamma} = 300 \text{ s}^{-1}$ for 60 s each, followed by an equilibration for 180 s. The steady-state viscosity is measured in the shear rate range of $\dot{\gamma} = 0.01 - 100 \text{ s}^{-1}$ first by gradually lowering $\dot{\gamma}$ from 100 to 0.01 s^{-1} , and then increasing it back up to 100 s^{-1} . To obtain the storage modulus G' and the loss modulus G'' , a frequency

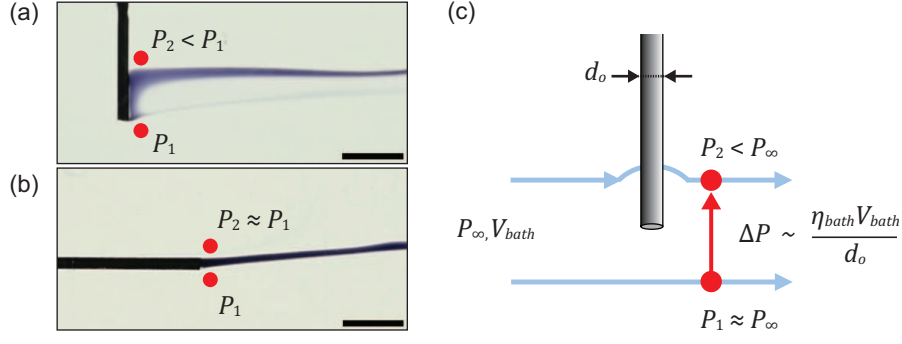


FIG. 3. Deposition of water threads in a glycerol bath that moves to the right at a constant speed $V_{bath} = 5.0 \text{ mm s}^{-1}$ from (a) a vertically oriented needle and (b) a horizontally oriented needle. The upward ink flow behind the vertically oriented needle indicates a pressure gradient ($P_1 > P_2$) in the direction parallel to the needle axis. Scale bar represents 5 mm. (c) Schematic of the streamlines above and below the needle tip. For a flow dominated by the viscous effects, the pressure difference in the needle direction ($\Delta P = P_1 - P_2$) scales as the viscosity of the bath fluid η_{bath} .

sweep is performed at a strain amplitude $\gamma_0 = 0.005$ and an amplitude sweep at a frequency $\omega = 6.28 \text{ rad s}^{-1}$. Both experiments are conducted to ensure frequency independence and linearity of the moduli. For the characterization of the transient viscoelasticity during recovery, we first run a shear start-up step at a constant shear rate $\dot{\gamma} = 0.01, 0.1, 1.0 \text{ s}^{-1}$ up to the total strain of $\gamma = 1.0$, at which the stress σ_0 is set to zero. The strain response during the resulting fluid-to-solid transition is used to estimate the transient elastic modulus and the transient viscosities. All experiments are conducted at room temperature $T = 21^\circ\text{C}$.

III. RESULTS

A. Dependence of penetration length on bath concentration and speed

The penetration length l depends on both the microgel concentration c of the bath fluid and the bath translation speed V_{bath} , as shown in Fig. 2(a,b). At lower concentrations, the penetration length l increases with c , while for higher c , l moderately decreases. At a given concentration, l decreases nearly monotonically with the bath speed V_{bath} , although its dependence on V_{bath} is less pronounced than that on c . We attribute this trend to the varying viscoelasticity and the yield stress of Carbopol suspensions in different concentration regimes. No spreading is observed when $V_{bath} = 0 \text{ mm s}^{-1}$, which indicates that this phenomenon is not caused by the wetting of the needle by the ink.

B. Viscous pressure drop in shear-thinning fluid baths

To elucidate the ink spreading at lower bath concentrations, where the shear-thinning fluid exhibits no solidlike

elasticity and yield stress, we first note that the spreading is observed even in a bath of glycerol, a Newtonian fluid, as shown in Fig. 3(a). Such upward flow of the ink is not observed when the orientation of the needle is parallel to the direction of bath displacement [26], although the dispensed ink far from the needle slowly but continuously rises due to buoyancy, hence slanting the filament, as displayed in Fig. 3(b). This absence of strong vertical ink flow right behind the needle suggests that the pressure right below the tip (P_1) is approximately equal to the pressure right above the tip (P_2) as expected from the symmetry of the flow. By contrast, the asymmetry between the flow above and below the tip when the needle is perpendicular to the bath displacement causes P_2 to be lower than P_1 , as illustrated in Fig. 3(a), leading to the vertical flow of the ink.

The pressure gradient in the vertical direction in the

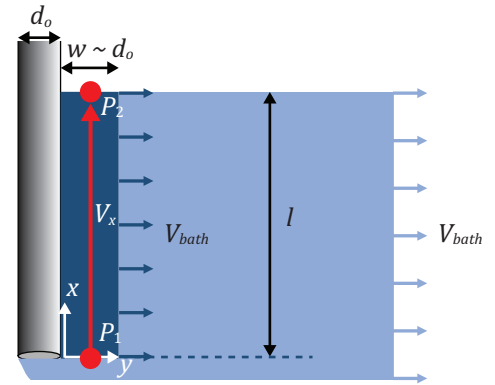


FIG. 4. Schematic illustrating the spreading ink flow due to viscous pressure drop across the needle. The vertical flow is assumed to occur within a column (dark blue) of width $w \sim d_o$ in both y and z directions, where d_o denotes the outer diameter of the needle. As the bath moves at a constant speed V_{bath} , a uniform outflow at V_{bath} occurs across the penetration length l .

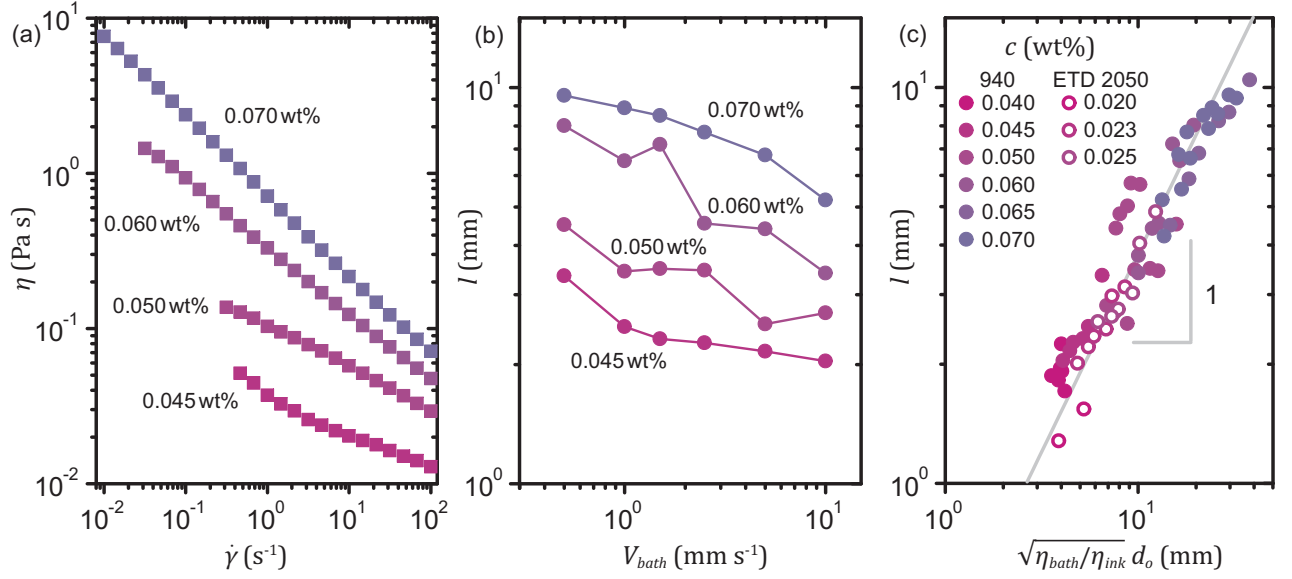


FIG. 5. (a) Apparent viscosity η of Carbopol 940 suspensions as a function of the shear rate $\dot{\gamma}$ for different particle concentrations c , where no yield stress is observed. (b) Penetration length l as a function of the bath speed V_{bath} for the corresponding c . (c) Linear scaling relation between l at various bath speeds V_{bath} and the square root of the viscosity ratio $\sqrt{\eta_{bath}/\eta_{ink}}$ for low- c Carbopol 940 and ETD 2050 suspensions, whose yield stresses are zero.

Newtonian fluid bath results from the viscous pressure drop across the needle. For fluid elements traveling around the cylinder, the friction from the outer surface dissipates mechanical energy through viscosity, which leads to a pressure drop downstream. A scaling relation derived from the Stokes equation $\mathbf{0} = -\nabla p + \eta_{bath} \nabla^2 \mathbf{v}_{bath}$ dictates that the pressure drop

$$P_\infty - P_2 \sim \frac{\eta_{bath} V_{bath}}{d_o}, \quad (1)$$

where p denotes the pressure field, η_{bath} the bath fluid viscosity, \mathbf{v}_{bath} the velocity field, P_∞ the far-field pressure and d_o the outer diameter of the needle. For fluid elements traveling below the needle, however, the local velocity field remains nearly the same as the upstream uniform flow, which suggests that $P_1 \approx P_\infty$. The pressure decrease $\Delta P \equiv P_1 - P_2$ in the upward direction behind the needle can therefore be expressed as

$$\Delta P \sim \frac{\eta_{bath} V_{bath}}{d_o}, \quad (2)$$

as illustrated in Fig. 3(c). The pressure difference due to gravity between the two points is neglected in this relation, since its effect is canceled out by the hydrostatic pressure gradient in the surrounding fluid.

When this viscous pressure drop in the Newtonian bath fluid generates the vertical flow of the ink, the penetration length l scales as the square root of the bath-to-ink viscosity ratio. Given the pressure set by the surrounding bath fluid, a column of the dispensed ink fluid forms right behind the needle, whose end pressures are equal to P_1 and P_2 , as shown in Fig. 4. Assuming that both horizontal dimensions of the ink column are of the order

of the needle outer diameter d_o , we derive a scaling relation from the steady-state momentum equation along the needle:

$$\frac{\Delta P}{l} \sim \frac{\eta_{ink} V_x}{d_o^2}, \quad (3)$$

where V_x denotes the characteristic ink velocity in the needle direction. Since the bath translates at a constant speed V_{bath} driving ink out of the column in which the upward flow occurs, the mass conservation holds when

$$V_x d_o^2 \sim V_{bath} l d_o. \quad (4)$$

Rearranging Eqs. (2)(3), and (4), yields

$$l \sim \sqrt{\frac{\eta_{bath}}{\eta_{ink}}} d_o, \quad (5)$$

which reflects that the spreading is driven by the bath fluid viscosity η_{bath} but is resisted by the ink fluid viscosity η_{ink} .

This competition between the opposing effects of the viscosities of the two fluids accounts for the ink spreading in the shear-thinning Carbopol suspensions. The viscosity η of Carbopol suspensions increases with the microgel concentration c and decreases with the shear rate $\dot{\gamma}$, as shown in Fig. 5(a), when c is kept sufficiently small such that no yield stress is observed. Thus, given the same ink fluid, it can be inferred from Eq. (5) that the penetration length l increases with c and decreases with the bath speed V_{bath} , as verified by the experimental results displayed in Fig. 5(b) and previously in Fig. 2(a). Evaluating the right-hand side of Eq. (5), using the values of η_{bath} corresponding to the effective shear rates $\dot{\gamma}_e \equiv V_{bath}/d_o$

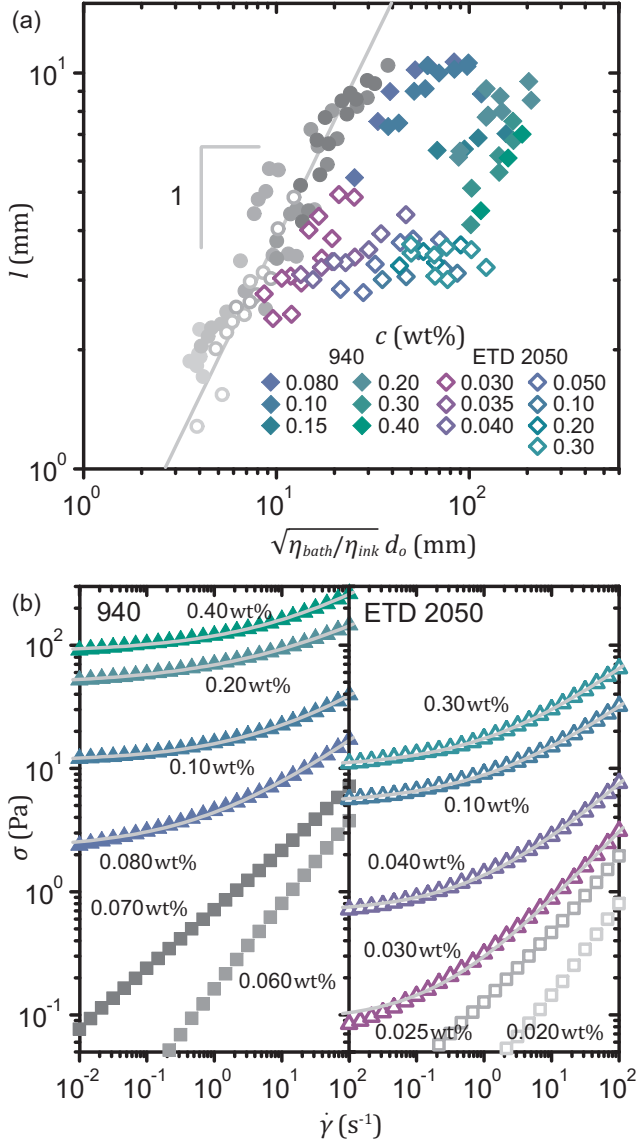


FIG. 6. (a) Deviation from the linear scaling relation between l and $\sqrt{\eta_{bath}/\eta_{ink}} d_o$ for higher- c Carbopol suspensions (colored). (b) Flow curves of the higher Carbopol concentrations (colored) that exhibit nonzero yield stresses. Grey lines represent the Herschel-Bulkley model fitted to the data for each concentration. The flow curves at lower concentrations (grey squares) do not form plateaus at low shear rates $\dot{\gamma}$.

indeed leads to a linear relationship between the measured penetration length l and $\sqrt{\eta_{bath}/\eta_{ink}} d_o$ for both types of Carbopol particles, as shown in Fig. 5(c), which validates the application of the Newtonian fluid model to the flow behavior in the shear-thinning fluids.

C. Viscoelastic pressure drop in yield stress fluid baths

In bath fluids of higher microgel concentrations, where nonzero yield stress is observed, the ink spreading cannot be solely attributed to the pressure drop across the

needle due to the bath fluid viscosity. The penetration length l does not increase linearly with $\sqrt{\eta_{bath}/\eta_{ink}} d_o$ at the higher concentrations, as shown in Fig. 6(a). For either Carbopol 940 or Carbopol ETD 2050, this deviation from the scaling in Eq. (5) occurs at the concentrations where the corresponding flow curves can be approximated by the Herschel-Bulkley model $\sigma = \sigma_y + K\dot{\gamma}^n$, where σ denotes the shear stress, σ_y the yield stress, K the consistency index, and n the power-law exponent [45], as displayed in Fig. 6(b). A nonzero value of the yield stress σ_y signifies jamming of the microgel particles in the bath, which gives rise to a solidlike elastic stress field due to the deformation caused by the translating needle [41]. We therefore hypothesize that the ink spreading in the yield stress fluid stems from a pressure gradient due to both the viscosity and the elasticity of the Carbopol suspensions.

The ink spreading due to the viscoelasticity of the yield stress fluid warrants a characterization of its transient rheological behavior, rather than its steady-state behavior, as the bath fluid constantly undergoes a fluid-to-solid transition behind the needle. During the translation, the bath fluid is locally yielded and fluidized in a confined region around the needle [9, 32–34]. The bath fluid then quickly recovers the yield stress in the areas where the needle has passed, as illustrated in the schematic of Fig. 7(a). Hence, any bath fluid element traveling adjacent to the needle undergoes a change of state from fluid to solid in the region behind the needle, where the ink column forms.

We examine the viscoelasticity of the bath fluid during its fluid-to-solid transition by performing an analogous experiment on the rheometer. In each experiment, the Carbopol suspension is sheared at a constant shear rate $\dot{\gamma}$ up to a total strain $\gamma = 1.0$, at which the sample is released by applying zero stress $\sigma = 0$ Pa. The total strain value of $\gamma = 1.0$ is chosen based on the assumption that the maximum shear strain observed in the fluidized region during printing is of the order of 1. However, we confirm that similar results are obtained even with a much larger strain $\gamma = 10$. The resolidification behind the needle is simulated by the subsequent constrained recovery of the strain γ while the stress is set to zero, a commonly used method to probe transient viscoelastic properties of various yield stress fluids [46]. We also find that the results depend only marginally on the initial shear rate within the range of $\dot{\gamma} = 0.01 - 1.0$ s^{-1} , and thus simply use the data obtained at $\dot{\gamma} = 1.0$ s^{-1} for each bath fluid in the following analysis.

We parameterize the viscoelastic behavior during the constrained recovery by fitting the transient response of the Jeffreys model, derived in Appendix A, to the strain as a function of time. A linear, three-parameter analog model that constitutes a serial connection of a viscoelastic solid part and a viscous fluid part [47–49], the Jeffreys model serves as a reasonable approximation of the temporal change in the strain, as illustrated in Fig. 7(b). The Jeffreys model is a simplest model that can mimic

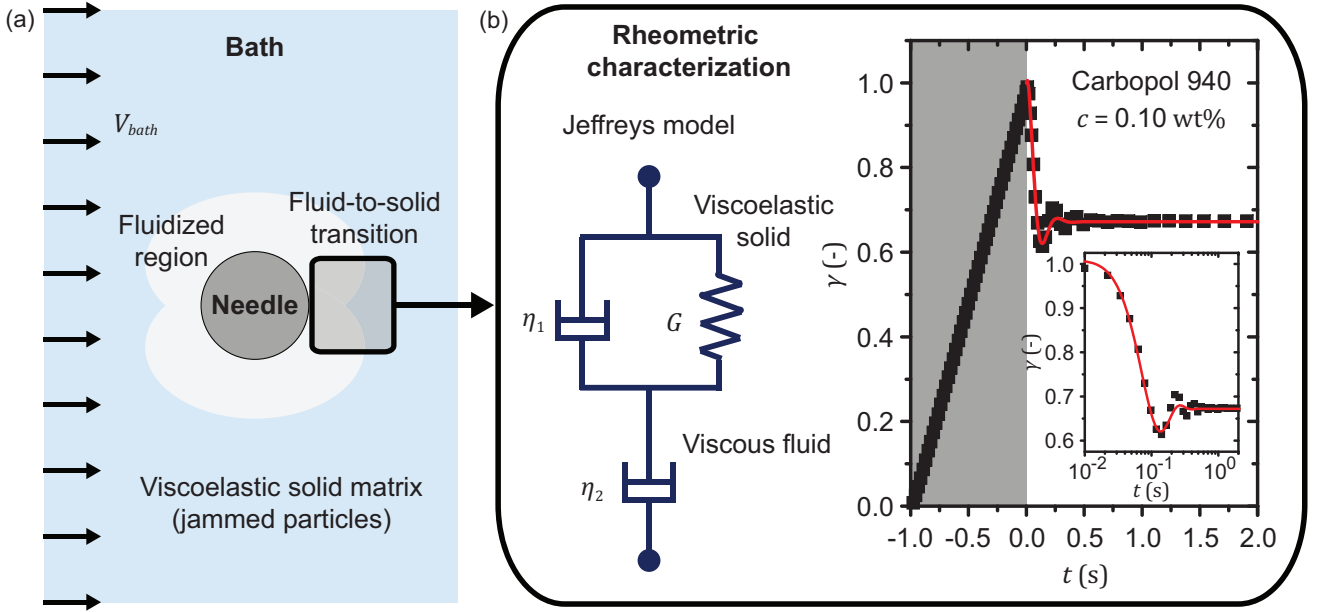


FIG. 7. (a) Top-view schematic of a Carbolpol bath around the needle. The yield stress fluid is locally fluidized upstream right in front of the needle and solidified downstream right behind the needle, forming a fluidized region (white) through which the ink can spread. (b) Rheometric characterization via constrained recovery experiments that mimic the fluid-to-solid transition behind the needle. The Jeffreys model, a 3-parameter viscoelastic analog model, is fitted to the strain response $\gamma(t)$ when the stress is set to zero, as shown by the red line. Inset: $\gamma(t)$ plotted on the log timescale.

a partial, delayed strain recovery with viscoelastic oscillations [48], and has been used to describe a transient behavior of Carbolpol suspensions [49]. The values of the two viscosities η_1 and η_2 and the elastic modulus G , obtained from the curve fits, reveal both similarities and differences between the steady-state and the transient rheology of Carbolpol suspensions, as described in Appendix B.

To account for the effects of the bath fluid viscoelasticity on the ink spreading, we estimate the penetration length induced by the viscous pressure drop and that by the elastic deformation separately. By replacing the steady-state viscosity η_{bath} in Eq. (5) with the transient viscosity η_2 of the viscous fluid part of the Jeffreys model, we expect the penetration length caused by the viscous pressure drop across the needle to be

$$l_v \sim \sqrt{\frac{\eta_2}{\eta_{ink}}} d_o. \quad (6)$$

We speculate that the pressure difference along the ink column due to the elastic stress applied by the surrounding solid matrix is of the order of

$$\Delta P \sim G\gamma_c \sim G, \quad (7)$$

where the characteristic shear strain γ_c is assumed to be 1, given a single geometric length scale d_o in the plane perpendicular to the needle. When combined with Eqs. (3) and (4), Eq. (7) yields the following scaling relation for the penetration length caused by the bath fluid

elasticity:

$$l_e \sim \sqrt{\frac{Gd_o}{\eta_{ink}V_{bath}}} d_o. \quad (8)$$

Although Eq. (6) is independent of the bath speed V_{bath} because the transient viscosity η_2 is independent of the shear rate, the elastic contribution to the spreading expressed in Eq. (8) incorporates the V_{bath} dependence of the penetration length l .

The resulting estimates of the viscous and the elastic penetration lengths, l_v and l_e respectively, indicate that the pressure difference due to the elasticity is indeed comparable to the viscous pressure drop for the high Carbolpol concentrations at or above the jamming transition. The values of l_v and l_e calculated with the transient viscoelastic parameters are of the same order as displayed in Fig. 8(a,b). As l_e increases more rapidly with the concentration c than l_v for either Carbolpol type, l_e even exceeds l_v at the highest concentrations. Neither dominates the other within the concentration ranges investigated in this work, however, which obscures how exactly the measured penetration length l depends on l_v and l_e .

Greater than the corresponding penetration length l approximately by an order of magnitude, the values of l_v and l_e also hint that the spreading is hindered at the high Carbolpol concentrations despite the combined effects of viscoelasticity. We ascribe the hindrance to the yield stress. When the yield stress relative to the viscous stress, as quantified by the Oldroyd number $Od \equiv \sigma_y / (K\dot{\gamma}^n)$ based on the Herschel-Bulkley model parameters, increases, the volume of the region of fluidization

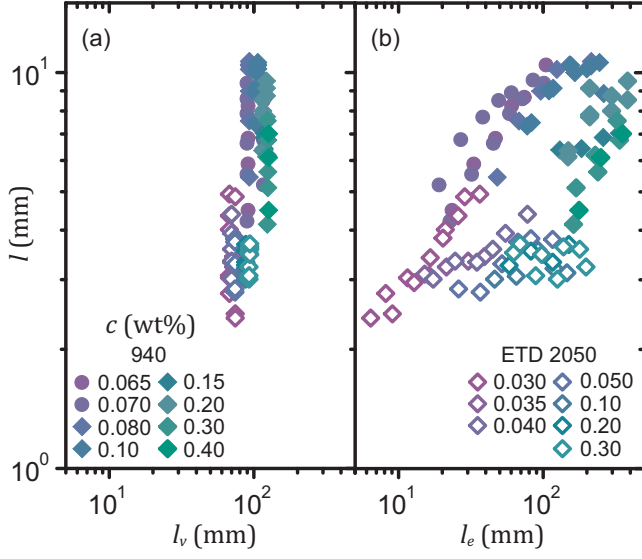


FIG. 8. Penetration length l at various bath speeds V_{bath} as a function of (a) the viscous penetration length scale l_v and (b) the elastic penetration length scale l_e for high Carbowol concentrations.

around the needle is known to decrease [9, 33, 50–52]. The reduced volume of the fluidized Carbowol suspension would suppress the elongation of the ink column, hence decreasing the penetration length. We find that the Oldroyd number $Od = \sigma_y / (K\dot{\gamma}_e^n)$ is of order 1 for most of the Carbowol suspensions with nonzero yield stresses, as shown in Appendix C, suggesting nonnegligible influence of the yield stress on the local flow around the needle. The interplay between the yield stress and the viscoelastic forces in determining the penetration length remains to be explored.

D. Defects at low and high microgel concentrations

Though our results indicate that the penetration length l is reduced when the concentration is much lower or much higher than the critical concentration at jamming for either type of Carbowol, printing the low-viscosity ink in bath fluids at such extreme concentrations is susceptible to the formation of other structural defects. At very low Carbowol concentrations, the viscosity of the suspension is of the same order of magnitude as the viscosity of water (~ 1 mPa s) as the microgel particles minimally interact with one another under shear. The inertia of the ink fluid injected into such a low-viscosity bath is not negligible even for the lowest injection speed $V_{ink} = 0.5$ mm s $^{-1}$ in our experiments. The corresponding Reynolds number $Re \equiv \rho V_{ink} d_i / \eta_{bath} \approx 0.5$, where $\rho = 1000$ kg m $^{-3}$ denotes the density of water, is of order 1. Furthermore, given $V_{ink} = V_{bath}$, $Re \approx 1$ indicates that the vorticity generated within the bath fluid around the translating needle can be advected over a considerable distance without dissipation, thus deforming the deposited ink filament. The structure of the printed ink

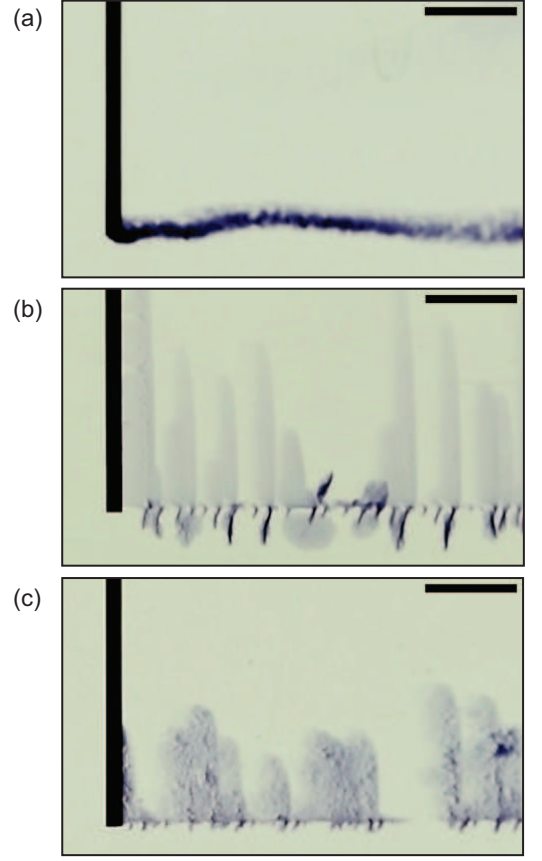


FIG. 9. Structural defects of deposited filaments at extreme Carbowol concentrations. (a) Bent filament in a dilute Carbowol 940 suspension ($c = 0.03$ wt%), and traces left by the intermittent bursts of the injected ink in (b) a dense Carbowol 940 suspension ($c = 0.30$ wt%), and (c) a dense Carbowol ETD 2050 suspension ($c = 0.30$ wt%), all at a bath speed $V_{bath} = 0.5$ mm s $^{-1}$. Each scale bar denotes 5 mm.

filament is indeed unstable, as shown in Fig. 9(a).

At high Carbowol concentrations, the ink is injected intermittently, as displayed in Fig. 9(b,c). Although the finger-like shape of the spread ink may be reminiscent of the Saffman-Taylor instability observed in quasi-2D geometries [53, 54], this phenomenon differs from the Saffman-Taylor instability in that the structures emerge from intermittent injection rather than an unstable translating interface. Also, this defect cannot be ascribed to any fracture or cavity formation in the Carbowol suspension, as no evidence of cavities within the bath is observed.

The unsteadiness of the ink flow arises from the yield stress of the bath fluid that results in a stress buildup within the injection system via the radial expansion of the soft tubing that connects the syringe and the injection needle. For such high concentrations, the yield stress σ_y of the Carbowol suspension is significantly high, such that the portion of the bath fluid underneath the tip of the moving needle does not continuously fluidize [44, 55]. In fact, the yield stress σ_y for the concentration $c = 0.10$ wt% at which the intermittent flow starts

to be observed, as shown in Fig. 2(b) for Carbopol 940, is approximately 10 Pa, sufficiently large to induce considerable expansion of the tubing during the continuous injection of the ink from the syringe. The increase in the radius δ_r due to an internal pressure increment Δp can be evaluated using the theory of linear elasticity for thin-walled tubes as $\delta_r = \Delta p R^2 / (hE)$, where R denotes the original tube radius, h the wall thickness, and E the Young's modulus. This radial expansion would increase the cross-sectional area by $2\pi R \delta_r = 2\pi \Delta p R^3 / (hE)$, which requires the ink to be injected into the tubing (but not yet into the bath) for the lag time $\Delta t \approx 2\pi \Delta p R^3 L / (hE Q_{ink})$, where L denotes the tubing length, Q_{ink} the volumetric flow rate. We estimate the distance traveled by the needle during the lag time to be

$$V_{bath} \Delta t = 8 \Delta p R^3 L / (h E d_i^2) \approx 0.90 \text{ mm}, \quad (9)$$

when $\Delta p = \sigma_y \approx 10$ Pa, comparable to the needle outer diameter $d_o = 0.908$ mm. For our polyvinyl chloride tubing, $R \approx 1.99$ mm, $L \approx 1.0$ m, $h = 0.794$ mm, and $E \approx 2.4$ MPa. At the high concentrations, it is therefore energetically more favorable for the pressurized ink to radially expand the tubing than to be injected into the bath, until the pressure inside the tubing increases by the yield stress, which takes longer time than the one required for the needle to traverse its own diameter. Increasing the bath speed V_{bath} , and thus the injection speed $V_{ink} = V_{bath}$, tends to suppress the bursts, as displayed in Fig. 2(b), which suggests that the higher shear stress applied by the more rapidly translating needle to the surrounding bath fluid facilitates yielding of the Carbopol suspension around the needle tip. The minimum bath speed required for a stable ink flow increases with the concentration, as the yield stress increases.

IV. DISCUSSION AND CONCLUSIONS

By dispensing water threads in baths of Carbopol suspensions, we show that the ink spreading, a unique type of defect commonly observed in embedded printing, results from the pressure gradient in the needle direction set by the viscoelasticity of the bath fluid. For low concentration Carbopol suspensions that exhibit shear thinning without yielding, the penetration length of the ink behind the needle scales as the square root of the bath-to-ink viscosity ratio at the corresponding effective shear rate, because of the pressure field generated by the viscous flow around the needle. For high concentration Carbopol suspensions that behave like soft solids due to their nonzero yield stresses, the stress around the needle due to the elastic modulus is comparable to the viscous pressure difference. Hence, the dependence of the penetration length on the Carbopol concentration and the bath speed can be better understood as the combined effects of the elasticity and the viscosity. The local fluidization and resolidification of the bath fluid around the needle for high Carbopol concentrations warrant a characterization of the

viscoelasticity during the fluid-to-solid transition. We parameterize the transient viscoelasticity by fitting the Jeffreys model to the strain response in constrained recovery experiments. We find that the viscous and elastic pressure gradients estimated by the transient viscoelastic parameters are of comparable scales, and hence neither viscosity nor elasticity alone fully accounts for the penetration length at and above the jamming transition. The values of the penetration length for the high Carbopol concentrations, however, are an order of magnitude lower than the expected length scales based on the viscoelasticity, which may be attributed to the reduced area of fluidization behind the needle due to the high yield stress.

These results suggest that the spreading of the low-viscosity ink can be best mitigated by utilizing baths at either very low or very high Carbopol concentrations. Yet the baths at very low concentrations fail to stabilize the dispensed ink as they cannot effectively dissipate the fluid kinetic energy, while the baths at very high concentrations suffer unsteady ink flow caused by the competition between the high yield stress and the elastic stress in the elastomer injection tubing. The presence of these distinct artifacts highlights that there are optimal levels of the viscosity and the yield stress of the bath fluid at which the deposition of the low-viscosity ink is best controlled in embedded printing. The challenge in preparing the optimal bath lies in that the viscosity and the yield stress (and the elasticity) cannot be independently tuned for most complex fluids.

A deeper understanding of the interactions between the ink and the bath fluids may be obtained by the flow visualization around the needle and the incorporation of extra rheological parameters in the model. Our model in this work accounts for only the ink flow in the vertical direction behind the needle. Experimental characterization of the ink flow at the needle tip upon its injection would add another dimension to the model, which may elucidate the role of the shear applied by the surrounding bath fluid or the mechanism for the intermittent bursts at higher Carbopol concentrations. A 3D visualization of the bath fluid would support or refute the hypothesis on the reduction of the fluidized area for higher Carbopol concentrations. The translation of the needle through the bath may induce local extensional flows behind the needle, in which the extensional viscosity of the bath fluid may come into play [56, 57]. Even the part of the bath fluid in shear flow may alter the pressure gradient in the ink column via its normal stress due to its non-Newtonian nature [58]. Our findings provide a good starting point for the development of more advanced models through such investigations.

ACKNOWLEDGMENTS

We acknowledge support from the University of California Cancer Research Coordinating Committee. We thank Lubrizol for generously providing the Carbopol

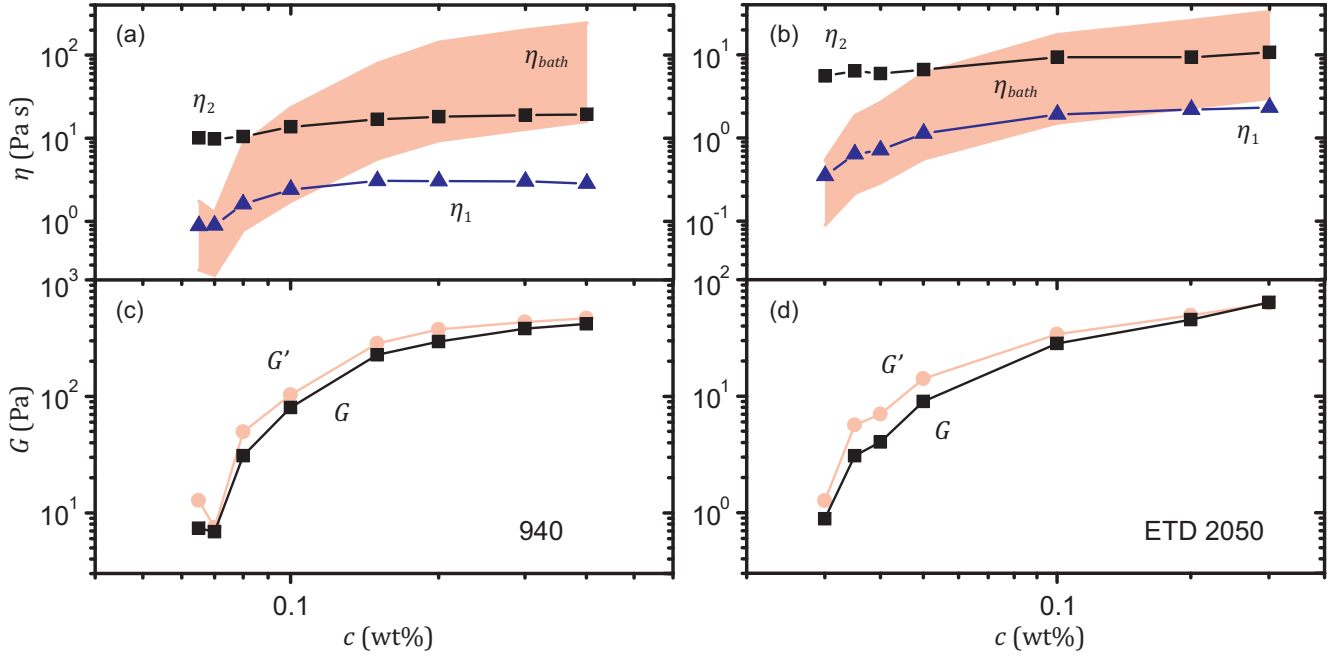


FIG. 10. (a,b) Comparison of the transient Jeffreys viscosities η_1 , η_2 and the steady-state apparent viscosity η_{bath} and (c,d) that of the transient Jeffreys elastic modulus G and the storage modulus G' at a frequency $\omega = 6.28 \text{ rad s}^{-1}$ for Carbopol 940 (a,c) and Carbopol ETD 2050 (b,d) suspensions at different concentrations. The shaded areas in (a) and (b) represent the ranges of η_{bath} for the shear rate $\dot{\gamma} = 0.55 - 11 \text{ s}^{-1}$, which corresponds to the range of the effective shear rates $\dot{\gamma}_e = V_{bath}/d_o$ for the bath speeds ($0.5 - 10 \text{ mm s}^{-1}$) used in this work.

samples.

Appendix A: Calculation of Jeffreys parameters from constrained recovery experiments

The functional form of the strain $\gamma(t)$ of the Jeffreys model in constrained recovery can be derived by directly solving for the strain term in the momentum equation for the rotating body of the stress-controlled rheometer and the stress-strain constitutive equation for the model [47–49]. In our experiments, in which the rheometer applies zero stress for $t \geq 0$, Newton's second law applied to the combined mass of the instrument and the upper plate dictates that

$$\frac{I}{b} \ddot{\gamma}(t) = [1 - H(t)] \sigma_0 - \sigma_s(t), \quad (\text{A1})$$

where I denotes the rotational inertia of the instrument and the geometry, b the geometry factor that converts the angular displacement and the torque to the strain and the stress, respectively, $H(t)$ the Heaviside function, σ_0 the steady-state stress applied by the rheometer during the flow at $t < 0$, and σ_s the stress applied to the sample. Note that σ_s is not necessarily zero for $t > 0$, as the instrument accelerates. For a plate-plate geometry, $b = \pi R^4/(2h)$, where R is the plate radius and h the gap size [48]. The constitutive relation for the Jeffreys model can be expressed as

$$(\eta_1 + \eta_2) \dot{\sigma}_s(t) + G \sigma_s(t) = \eta_2 G \dot{\gamma}(t) + \eta_1 \eta_2 \ddot{\gamma}(t), \quad (\text{A2})$$

where η_1 , η_2 , and G denote the model parameters, as shown in the schematic of Fig. 7(b).

Substituting the expression for $\ddot{\gamma}$ from Eq. (A1) into Eq. (A2) and differentiating with respect to time leads to

$$\begin{aligned} (\eta_1 + \eta_2) \ddot{\sigma}_s + \left(G + \frac{\eta_1 \eta_2 b}{I} \right) \dot{\sigma}_s + \frac{\eta_2 G b}{I} \sigma_s \\ = -\frac{\eta_2 G b}{I} \sigma_0 H(t) - \frac{\eta_1 \eta_2 b}{I} \sigma_0 \delta(t) + \frac{\eta_2 G b}{I} \sigma_0, \end{aligned} \quad (\text{A3})$$

where δ denotes the Dirac delta function. By solving for the sample stress $\sigma_s(t \geq 0)$ in the Laplace domain with a set of initial conditions $\sigma_s(t = 0^-) = \sigma_0$ and $\dot{\sigma}_s(t = 0^-) = 0$, it can be expressed as

$$\sigma_s(t) = \sigma_0 \exp(-Bt) [\cos(At) + C \sin(At)], \quad (\text{A4})$$

where

$$A = \frac{\sqrt{-(GI - \eta_1 \eta_2 b)^2 + 4GI\eta_2^2 b}}{2(\eta_1 + \eta_2)I} \quad (\text{A5})$$

$$B = \frac{GI + \eta_1 \eta_2 b}{2(\eta_1 + \eta_2)I} \quad (\text{A6})$$

$$C = \frac{GI - \eta_1 \eta_2 b}{\sqrt{-(GI - \eta_1 \eta_2 b)^2 + 4GI\eta_2^2 b}}. \quad (\text{A7})$$

Substituting Eq. (A4) into Eq. (A1) and integrating twice

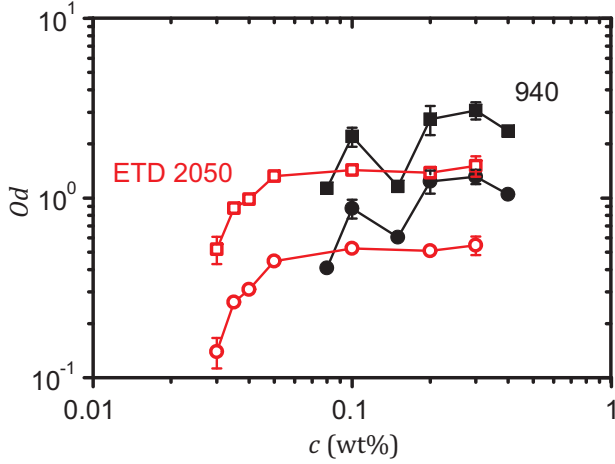


FIG. 11. Oldroyd number Od at the effective shear rates $\dot{\gamma}_e = V_{bath}/d_o$ corresponding to $V_{bath} = 1.0 \text{ mm s}^{-1}$ (squares) and $V_{bath} = 10.0 \text{ mm s}^{-1}$ (circles) as a function of the Carbopol concentration c for Carbopol 940 (black filled symbols) and Carbopol ETD 2050 (red open symbols).

for $t > 0$ yields

$$\gamma(t) = -\frac{b\sigma_0}{I(A^2 + B^2)^2} \exp(-Bt) [X_1 \cos(At) - X_2 \sin(At)] + \frac{b}{I} K_1 t + \frac{b}{I} K_2, \quad (\text{A8})$$

where

$$X_1 = B^2 - A^2 + 2ABC \quad (\text{A9})$$

$$X_2 = A^2 C - B^2 C + 2AB, \quad (\text{A10})$$

and K_1 and K_2 denote constants of integration. Since the strain has to reach a constant value as $t \rightarrow \infty$, K_1 is assumed to be zero. After calculating the value of K_2 from the late-time plateau of the strain $\gamma(t)$ in the experiments, we fit a curve of the functional form in Eq. (A8)

to the experimental $\gamma(t)$ while imposing the initial condition $\gamma(t = 0) = 1.0$ to ensure continuity of the strain. Using Eqs. (A5)-(A10), we calculate the Jeffreys parameters η_1 , η_2 , and G , as well as the steady-state stress σ_0 . We confirm the validity of the fitting results by comparing the value of σ_0 to that of the actual stress applied just prior to the application of zero stress.

Appendix B: Comparison of transient and steady-state rheological parameters

Although both transient viscosities η_1 and η_2 tend to increase with the microgel concentration c for either Carbopol type, their concentration dependence is much weaker than that of the steady-state viscosity η_{bath} , as displayed in Fig. 10(a,b). This pronounced difference may arise from that the steady-state viscosity originates in constant shearing and resultant deformation of particles out of equilibrium, whereas the transient viscosities during the recovery characterize the transition back into equilibrium upon the removal of the shearing force. The transient elastic modulus G , by contrast, closely follows the steady-state storage modulus G' for all the concentrations of either Carbopol type, as shown in Fig. 10(c,d), which may likewise be attributed to the fact that the system remains close to mechanical equilibrium during the small-amplitude oscillatory shear. The storage modulus G' is nearly independent of the frequency ω for all the Carbopol suspensions.

Appendix C: Dependence of Oldroyd number Od on bath speed V_{bath} and concentration c

The Oldroyd number $Od = \sigma_y / (K \dot{\gamma}_e^n)$ is mostly of order 1 within the range of bath speeds V_{bath} studied in this work, as shown in Fig. 11. In addition, Od increases with the concentration c for both types of Carbopol, which may illuminate why the penetration length l tends to decrease with c for the highest concentrations.

-
- [1] M. A. Saadi, A. Maguire, N. T. Pottackal, M. S. H. Thakur, M. M. Ikram, A. J. Hart, P. M. Ajayan, and M. M. Rahman, Direct ink writing: A 3d printing technology for diverse materials, *Adv. Mater.* **34**, 2108855 (2022).
 - [2] Y. Liu, M. Hildner, O. Roy, W. A. V. den Bogert, J. Lorenz, M. Desroches, K. Koppi, A. Shih, and R. G. Larson, On the selection of rheological tests for the prediction of 3d printability, *J. Rheol.* **67**, 791 (2023).
 - [3] W. Wu, A. Deconinck, and J. A. Lewis, Omnidirectional printing of 3d microvascular networks, *Adv. Healthc. Mater.* **23**, H178 (2011).
 - [4] J. T. Muth, D. M. Vogt, R. L. Truby, Y. Mengüç, D. B. Kolesky, R. J. Wood, and J. A. Lewis, Embedded 3d printing of strain sensors within highly stretchable elastomers, *Adv. Mater.* **26**, 6307 (2014).
 - [5] T. Bhattacharjee, S. M. Zehnder, K. G. Rowe, S. Jain, R. M. Nixon, W. G. Sawyer, and T. E. Angelini, Writing in the granular gel medium, *Sci. Adv.* **1**, e1500655 (2015).
 - [6] K. J. LeBlanc, S. R. Niemi, A. I. Bennett, K. L. Harris, K. D. Schulze, W. G. Sawyer, C. Taylor, and T. E. Angelini, Stability of high speed 3d printing in liquid-like solids, *ACS Biomater. Sci. Eng.* **2**, 1796 (2016).
 - [7] C. S. O'bryan, T. Bhattacharjee, S. Hart, C. P. Kabb, K. D. Schulze, I. Chilakala, B. S. Sumerlin, W. G. Sawyer, and T. E. Angelini, Self-assembled micro-organogels for 3d printing silicone structures, *Sci. Adv.* **3**, e1602800 (2017).

- [8] C. B. Highley, K. H. Song, A. C. Daly, and J. A. Burdick, Jammed microgel inks for 3d printing applications, *Adv. Sci.* **6**, 1801076 (2019).
- [9] A. K. Grosskopf, R. L. Truby, H. Kim, A. Perazzo, J. A. Lewis, and H. A. Stone, Viscoplastic matrix materials for embedded 3d printing, *ACS Appl. Mater. Interfaces* **10**, 23353 (2018).
- [10] A. Lee, A. R. Hudson, D. J. Shiwardski, J. W. Tashman, T. J. Hinton, S. Yerneni, J. M. Bliley, P. G. Campbell, and A. W. Feinberg, 3d bioprinting of collagen to rebuild components of the human heart, *Science* **365**, 482 (2019).
- [11] N. Noor, A. Shapira, R. Edri, I. Gal, L. Wertheim, and T. Dvir, 3d printing of personalized thick and perfusable cardiac patches and hearts, *Adv. Sci.* **6**, 1900344 (2019).
- [12] L. Cai, J. Marthelot, and P. T. Brun, An unbounded approach to microfluidics using the rayleigh–plateau instability of viscous threads directly drawn in a bath, *Proc. Natl. Acad. Sci. U. S. A.* **116**, 22966 (2019).
- [13] T. Uchida and H. Onoe, 4d printing of multi-hydrogels using direct ink writing in a supporting viscous liquid, *Micromachines* **10**, 433 (2019).
- [14] Y. Jin, K. Song, N. Gellermann, and Y. Huang, Printing of hydrophobic materials in fumed silica nanoparticle suspension, *ACS Appl. Mater. Interfaces* **11**, 29207 (2019).
- [15] L. Ning, R. Mehta, C. Cao, A. Theus, M. Tomov, N. Zhu, E. R. Weeks, H. Bauser-Heaton, and V. Serpooshan, Embedded 3d bioprinting of gelatin methacryloyl-based constructs with highly tunable structural fidelity, *ACS Appl. Mater. Interfaces* **12**, 44563 (2020).
- [16] L. Friedrich and M. Begley, Changes in filament microstructures during direct ink writing with a yield stress fluid support, *ACS Appl. Polym. Mater.* **2**, 2528 (2020).
- [17] R. Xu, T. Liu, H. Sun, B. Wang, S. Shi, and T. P. Russell, Interfacial assembly and jamming of polyelectrolyte surfactants: A simple route to print liquids in low-viscosity solution, *ACS Appl. Mater. Interfaces* **12**, 18116 (2020).
- [18] M. E. Cooke and D. H. Rosenzweig, The rheology of direct and suspended extrusion bioprinting, *APL Bioeng.* **5**, 011502 (2021).
- [19] M. E. Prendergast and J. A. Burdick, Computational modeling and experimental characterization of extrusion printing into suspension baths, *Adv. Healthc. Mater.* **11**, 2101679 (2022).
- [20] Q. Wu, K. Song, D. Zhang, B. Ren, M. Sole-Gras, Y. Huang, and J. Yin, Embedded extrusion printing in yield-stress-fluid baths, *Matter* **5**, 3775 (2022).
- [21] L. M. Friedrich, R. T. Gunther, and J. E. Seppala, Simulated stress mitigation strategies in embedded bioprinting, *Phys. Fluids* **34**, 083112 (2022).
- [22] L. M. Friedrich, R. T. Gunther, and J. E. Seppala, Suppression of filament defects in embedded 3d printing, *ACS Appl. Mater. Interfaces* **14**, 32561 (2022).
- [23] M. Becker, M. Gurian, M. Schot, and J. Leijten, Aqueous two-phase enabled low viscosity 3d (lov3d) bioprinting of living matter, *Adv. Sci.* **10**, 2204609 (2023).
- [24] N. D. Arun, H. Yang, L. Yao, and A. W. Feinberg, Non-planar 3d printing of epoxy using freeform reversible embedding, *Adv. Mater. Technol.* **8**, 2201542 (2023).
- [25] S. Duraivel, D. Laurent, D. A. Rajon, G. M. Scheutz, A. M. Shetty, B. S. Sumerlin, S. A. Banks, F. J. Bova, and T. E. Angelini, A silicone-based support material eliminates interfacial instabilities in 3d silicone printing, *Science* **379**, 1248 (2023).
- [26] V. D. Trikalitis, N. J. Kroese, M. Kaya, C. Cofiño-Fabres, S. ten Den, I. S. Khalil, S. Misra, B. F. Koopman, R. Passier, V. Schwach, and J. Rouwkema, Embedded 3d printing of dilute particle suspensions into dense complex tissue fibers using shear thinning xanthan baths, *Biofabrication* **15**, 015014 (2023).
- [27] L. M. Friedrich and J. E. Seppala, Simulated filament shapes in embedded 3d printing, *Soft Matter* **17**, 8027 (2021).
- [28] P. K. Kundu, I. M. Cohen, and D. R. Dowling, *Fluid Mechanics*, 6th ed. (Elsevier, 2016).
- [29] S. Kenney, K. Poper, G. Chapagain, and G. F. Christopher, Large Deborah number flows around confined microfluidic cylinders, *Rheol. Acta* **52**, 485 (2013).
- [30] S. J. Haward, K. Toda-Peters, and A. Q. Shen, Steady viscoelastic flow around high-aspect-ratio, low-blockage-ratio microfluidic cylinders, *J. Nonnewton. Fluid Mech.* **254**, 23 (2018).
- [31] C. Li, B. Thomases, and R. D. Guy, Orientation dependent elastic stress concentration at tips of slender objects translating in viscoelastic fluids, *Phys. Rev. Fluids* **4**, 031301(R) (2019).
- [32] A. M. Putz, T. I. Burghlea, I. A. Frigaard, and D. M. Martinez, Settling of an isolated spherical particle in a yield stress shear thinning fluid, *Phys. Fluids* **20**, 033102 (2008).
- [33] D. L. Tokpavi, A. Magnin, and P. Jay, Very slow flow of bingham viscoplastic fluid around a circular cylinder, *J. Nonnewton. Fluid Mech.* **154**, 65 (2008).
- [34] D. L. Tokpavi, P. Jay, A. Magnin, and L. Josic, Experimental study of the very slow flow of a yield stress fluid around a circular cylinder, *J. Nonnewton. Fluid Mech.* **164**, 35 (2009).
- [35] J. M. Piau, Carbopol gels: Elastoviscoplastic and slippery glasses made of individual swollen sponges. meso- and macroscopic properties, constitutive equations and scaling laws, *J. Nonnewton. Fluid Mech.* **144**, 1 (2007).
- [36] M. Dinkgreve, M. Fazilati, M. M. Denn, and D. Bonn, Carbopol: From a simple to a thixotropic yield stress fluid, *J. Rheol.* **62**, 773 (2018).
- [37] E. Younes, M. Himl, Z. Stary, V. Bertola, and T. Burghlea, On the elusive nature of carbopol gels: “model”, weakly thixotropic, or time-dependent viscoplastic materials?, *J. Nonnewton. Fluid Mech.* **281**, 104315 (2020).
- [38] I. A. Gutowski, D. Lee, J. R. de Bruyn, and B. J. Frisken, Scaling and mesostructure of carbopol dispersions, *Rheol. Acta* **51**, 441 (2012).
- [39] T. Bhattacharjee, C. P. Kabb, C. S. O’bryan, J. M. Urueña, B. S. Sumerlin, W. G. Sawyer, and T. E. Angelini, Polyelectrolyte scaling laws for microgel yielding near jamming, *Soft Matter* **14**, 1559 (2018).
- [40] Z. Jaworski, T. Szychaj, A. Story, and G. Story, Carbomer microgels as model yield-stress fluids, *Rev. Chem. Eng.* **38**, 881 (2022).
- [41] C. Oelschlaeger, J. Marten, F. Périodont, and N. Willenbacher, Imaging of the microstructure of carbopol dispersions and correlation with their macroelasticity: A micro- and macro-rheological study, *J. Rheol.* **66**, 749 (2022).
- [42] R. M. Manglik, V. M. Wasekar, and J. Zhang, Dynamic and equilibrium surface tension of aqueous surfactant and polymeric solutions, *Exp. Therm. Fluid Sci.* **25**, 55 (2001).
- [43] J. Boujlel and P. Coussot, Measuring the surface tension of yield stress fluids, *Soft Matter* **9**, 5898 (2013).

- [44] H. Mohammadigoushki and K. Shoele, Cavitation rheology of model yield stress fluids based on carbopol, *Langmuir* **39**, 7672 (2023).
- [45] T. Divoux, C. Barentin, and S. Manneville, From stress-induced fluidization processes to herschel-bulkley behaviour in simple yield stress fluids, *Soft Matter* **7**, 8409 (2011).
- [46] P. K. Singh, J. C.-W. Lee, K. A. Patankar, and S. A. Rogers, Revisiting the basis of transient rheological material functions: Insights from recoverable strain measurements, *J. of Rheol.* **65**, 129 (2021).
- [47] C. Baravian, D. Quemada, C. Baravian, and D. Quemada, Using instrumental inertia in controlled stress rheometry, *Rheol. Acta* **37**, 223 (1998).
- [48] R. H. Ewoldt and G. H. McKinley, Creep ringing in rheometry or how to deal with oft-discarded data in step stress tests!, *Rheol. Bull.* **76**, 4 (2007).
- [49] G. Benmouffok-Benbelkacem, F. Caton, C. Baravian, and S. Skali-Lami, Non-linear viscoelasticity and temporal behavior of typical yield stress fluids: Carbopol, xanthan and ketchup, *Rheol. Acta* **49**, 305 (2010).
- [50] B. D. D. Besses, A. Magnin, and P. Jay, Viscoplastic flow around a cylinder in an infinite medium, *J. Nonnewton. Fluid Mech.* **115**, 27 (2003).
- [51] D. Fraggedakis, Y. Dimakopoulos, and J. Tsamopoulos, Yielding the yield-stress analysis: A study focused on the effects of elasticity on the settling of a single spherical particle in simple yield-stress fluids, *Soft Matter* **12**, 5378 (2016).
- [52] D. R. Hewitt and N. J. Balmforth, Viscoplastic slender-body theory, *J. Fluid Mech.* **856**, 870 (2018).
- [53] P. G. Saffman and G. Taylor, The penetration of a fluid into a porous medium or hele-shaw cell containing a more viscous liquid, *Proc. R. Soc. London Ser. A* **245**, 312 (1958).
- [54] G. M. Homsy, Viscous fingering in porous media, *Annu. Rev. Fluid Mech.* **19**, 271 (1987).
- [55] S. B. Hutchens, S. Fakhouri, and A. J. Crosby, Elastic cavitation and fracture via injection, *Soft Matter* **12**, 2557 (2016).
- [56] A. Z. Nelson, K. S. Schweizer, B. M. Rauzan, R. G. Nuzzo, J. Vermant, and R. H. Ewoldt, Designing and transforming yield-stress fluids, *Curr. Opin. Solid State Mater.Sci.* **23**, 100758 (2019).
- [57] R. H. Ewoldt and C. Saengow, Designing complex fluids, *Annu. Rev. Fluid Mech.* **54**, 413 (2022).
- [58] H. de Cagny, M. Fazilati, M. Habibi, M. M. Denn, and D. Bonn, The yield normal stress, *J. Rheol.* **63**, 285 (2019).